ELSEVIER

Journal of Biomechanics 36 (2003) 1185–1196

JOURNAL OF BIOMECHANICS

www.elsevier.com/locate/jbiomech
www.JBiomech.com

Hemodynamics simulation and identification of susceptible sites of atherosclerotic lesion formation in a model abdominal aorta

J.R. Buchanan[a,1], C. Kleinstreuer[a,*], S. Hyun[b], G.A. Truskey[c]

[a] *Department of Mechanical and Aerospace Engineering, North Carolina State University, Campus Box 7910, 3211 Broughton Hall, Raleigh, NC 27695-7910, USA*

[b] *Department of Biomedical Engineering, Mercer University, Macon, GA 31207, USA*

[c] *Biomedical Engineering Department, Duke University, Durham, NC 27708-0281, USA*

Abstract

Employing the rabbit's abdominal aorta as a suitable atherosclerotic model, transient three-dimensional blood flow simulations and monocyte deposition patterns were used to evaluate the following hypotheses: (i) simulation of monocyte transport through a model of the rabbit abdominal aorta yields cell deposition patterns similar to those seen in vivo, and (ii) those deposition patterns are correlated with hemodynamic wall parameters related to atherosclerosis. The deposition pattern traces a helical shape down the aorta with local elevation in monocyte adhesion around vessel branches. The cell deposition pattern was altered by an exercise waveform with fewer cells attaching in the upper abdominal aorta but more attaching around the renal orifices. Monocyte deposition was correlated with the wall shear stress gradient and the wall shear stress angle gradient. The wall stress gradient, the wall shear stress angle gradient and the normalized monocyte deposition fraction were correlated with the distribution of monocytes along the abdominal aorta and monocyte deposition is correlated with the measured distribution of monocytes around the major abdominal branches in the cholesterol-fed rabbit. These results suggest that the transport and deposition pattern of monocytes to arterial endothelium plays a significant role in the localization of lesions.

Keywords: Computational blood flow simulation; Rabbit aorta; Atherosclerotic model; Hemodynamic wall parameters; Monocyte deposition; Experimental data comparisons

1. Introduction

Atherosclerotic lesions appear most frequently in bends and junctions of medium to large arteries. Factors contributing to this degenerative disease include the individual's genetic make-up, diet and lifestyle as well as the local arterial hemodynamics (Olsson, 1987; Texon, 1996). Abnormal hemodynamic events, often labeled "disturbed flow", such as low wall shear stress (WSS) levels, high particle residence times, excessive arterial wall strains, and wall compliance mismatch, play important roles in the regulation of vascular biology and the localization of atherosclerosis (DeBakey et al., 1985; Nerem, 1992; Ross, 1993; Texon, 1996). Of all the hemodynamic factors which act directly on the endothelium, the WSS and its derivatives as well as the transport and vessel wall uptake of monocytes and lipoproteins are the most important ones related to the onset and distribution of atherosclerotic lesions (Davis et al., 1995; Frangos et al., 1999; Pedersen et al., 1999; Kleinstreuer et al., 2001).

The rabbit abdominal aorta is a suitable atherosclerotic model which closely mimics the human lesions if correct dietary conditions are applied (Zeindler et al., 1989; Bocan et al., 1993; Daley et al., 1994; Barakat et al., 1997; Barnes and Weinberg, 1998). Computational fluid-particle dynamics simulations can complement experimental observations in determining hemodynamic factors which encapsulate disturbed flow and cell deposition patterns, and identify local sites in the vascular system which are susceptible to the onset of atherosclerotic lesions (Kleinstreuer et al., 2001). For example, in normocholesterolemic rabbits (Herrmann et al., 1994; Truskey et al., 1999), the frequency of sites

*Corresponding author. Tel.: +1-919-515-5216; fax: +1-919-515-7968.

E-mail address: ck@eos.ncsu.edu (C. Kleinstreuer).

URL: http://www.mae.ncsu.edu/research/ck_CFPDlab/index.html.

[1] Current address: Bechtel Bettis, Inc., West Mifflin, PA 15122-0079, USA.

0021-9290/03/$ - see front matter
doi:10.1016/S0021-9290(03)00088-5

of elevated low-density-lipoprotein (LDL) permeability and the magnitude of permeability were greatest where lesions developed earliest after the onset of a hypercholesterolemic diet (Zeindler et al., 1989). In a subsequent study in normocholesterolemic rabbits, Malinauskas et al. (1995, 1998) showed that white blood cells showed a spatial correlation to the sites of elevated LDL permeability and did not show a correlation with replicating endothelial cells. In addition, in vitro (Hinds et al., 2001; Barber et al., 1998) and in situ studies (Ramos et al., 1999) indicate that the local flow field influences monocyte adhesion to endothelium. Hemodynamic simulations of three-dimensional flow around the rabbit celiac branch showed that the distribution of monocytes obtained by Malinauskas et al. (1995) was correlated with the WSS gradient (WSSG), but not with the oscillatory shear index (OSI) or the WSS (Buchanan et al., 1999). A limitation of their work is that only the celiac branch was modeled without other abdominal branches.

The goal of the current study is to test the following two hypotheses: (i) simulation of monocyte transport through a model of the rabbit abdominal aorta yields cell deposition patterns which are similar to those seen in vivo, and (ii) those deposition patterns are correlated with hemodynamic wall parameters (HWPs) which indicate sites of the onset of atherosclerosis. In order to test these hypotheses, we extend the work of Buchanan et al. (1999) in two important ways. First, we have included all of the major branches in the abdominal aorta segment of interest. Second, we also examine the importance of monocyte deposition onto arterial endothelium.

2. Materials and methods

Transient laminar three-dimensional blood flow in a model aorta (Fig. 1) was first simulated and analyzed. Then, typical HWPs describing disturbed flows, e.g., the time-averaged WSS, OSI, WSSG, WSS angle gradient (WSSAG), and monocyte deposition, were compared with measured data sets to test the two stated hypotheses. While two input pulses with controlled branch flow rate divisions were considered (Figs. 1a and b), results focus upon the resting pulse. The no-slip condition was invoked for the walls and zero pressure was assumed for the outlets. The flow inlet conditions are discussed below.

Assuming laminar incompressible flow of a non-Newtonian fluid in a smooth rigid conduit, the governing equations are (Kleinstreuer, 1997):

$$\text{continuity}: \quad \nabla \cdot \vec{u} = 0; \tag{1}$$

$$\text{momentum}: \quad \rho \frac{D\vec{u}}{Dt} = -\nabla p + \nabla \cdot \tau \tag{2}$$

The non-Newtonian blood rheology used in Eq. (2) is represented by

$$\vec{\vec{\tau}} = 2\eta(\mathrm{II}_D)\vec{\vec{D}}, \tag{3}$$

where II_D is the second invariant of the strain-rate tensor which is denoted by $\mathrm{II}_D = \frac{1}{2}[(tr\,\vec{\vec{D}})^2 + tr(\vec{\vec{D}})^2]$ and $\vec{\vec{D}} = \frac{1}{2}[\nabla\vec{u} + (\nabla\vec{u})^{\mathrm{T}}]$, while $\dot{\gamma} = 2\vec{\vec{D}}$ and $\eta(\dot{\gamma})$ is a function of the shear rate given by a Quemada model (Popel and Enden, 1993; Buchanan et al., 2000) as

$$\eta(\dot{\gamma}) = \left(\sqrt{\eta_\infty} + \frac{\sqrt{\tau_{\mathrm{ay}}}}{\sqrt{\lambda} + \sqrt{\dot{\gamma}}}\right), \tag{4}$$

where $\dot{\gamma}$ is the local shear rate, η_∞ is the asymptotic viscosity (0.02982 [dyn s/cm^2]), τ_{ay} is the apparent "yield" stress (0.2876 [dyn/cm^2]), and λ is an additional shear stress modifier (4.020 [1/s]).

Being situated sufficiently far downstream from the actual aortic arch, fully developed transient velocity profiles (Womersley, 1955) are assumed, following the resting pulse or exercise pulse (Fig. 1a) to form the inlet conditions.

For dilute suspensions of spherical non-rotating micro-particles, the trajectory equations can be written as (Kleinstreuer, 2003)

$$\frac{\mathrm{d}\vec{v}_{\mathrm{p}}}{\mathrm{d}t} = \alpha\frac{\mathrm{d}\vec{u}}{\mathrm{d}t} - \frac{\vec{v}_{\mathrm{p}} - \vec{u}}{\tau_{\mathrm{p}}} \tag{5}$$

and

$$\frac{\mathrm{d}\vec{x}_{\mathrm{p}}}{\mathrm{d}t} = \vec{v}_{\mathrm{p}}, \tag{6}$$

where $\vec{v}_{\mathrm{p}}$ is the particle velocity vector, $\vec{x}_{\mathrm{p}}$ is the particle position vector, $\alpha = \rho_{\mathrm{f}}/\rho_{\mathrm{p}}$ is the fluid-to-particle density ratio, and $\tau_{\mathrm{p}} = \rho_{\mathrm{p}}d_{\mathrm{p}}^2/18\mu$ is the particle relaxation time defined based on the particle diameter. Up to 50,000 non-interacting particles were released in the inlet plane following a time-dependent velocity distribution.

Specifically, the six-component stress tensor in Eq. (2) or Eq. (3) reduces to a two-component shear stress vector at the wall, and WSS is defined as

$$\tau \Rightarrow \vec{\tau}_{\mathrm{w}} = (\tau_{\mathrm{w,m}}, \tau_{\mathrm{w,n}}) \quad \text{and} \quad \mathrm{WSS} = \frac{1}{\tau_0}\frac{1}{T}\int_0^T |\vec{\tau}_{\mathrm{w}}|\,\mathrm{d}t, \tag{7a, b}$$

where T is the time period and τ_0 is the WSS for Poiseuille flow at the mean flow Reynolds number.

Employing the WSSG concept to represent locally disturbed flow, the non-dimensional value of the WSSG is defined as

$$\mathrm{WSSG} = \frac{D}{\tau_0}\frac{1}{T}\int_0^T \sqrt{\left(\frac{\partial\tau_x}{\partial x}\right)^2 + \left(\frac{\partial\tau_y}{\partial y}\right)^2 + \left(\frac{\partial\tau_z}{\partial z}\right)^2}\,\mathrm{d}t, \tag{8}$$

where D is the tube inlet diameter.

(a) Input Pulses for rabbits

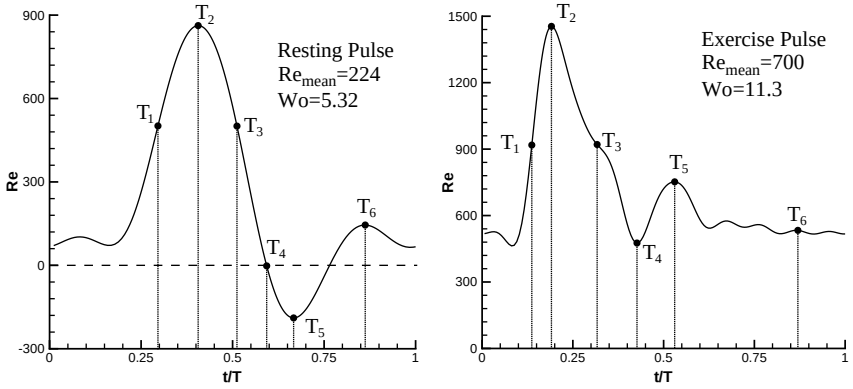

(b) Complete Abdominal Aorta with Inlet and Branch Flow Rate Divisions

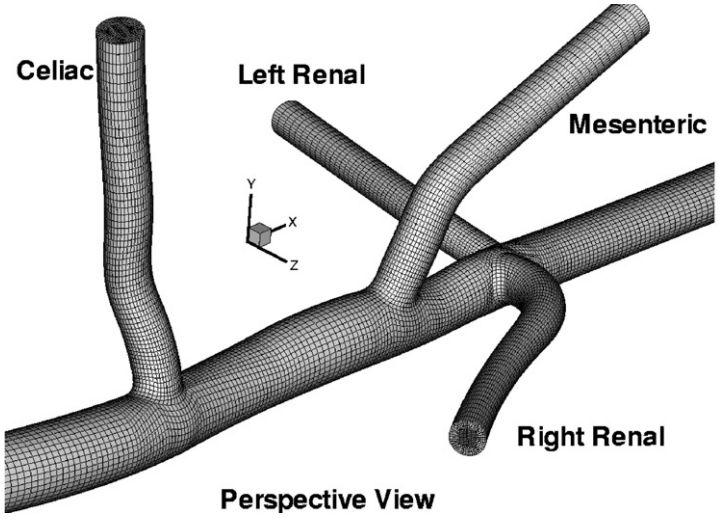

	Resting	Exercise
Q^*_c	0.31	0.11
Q^*_m	0.39	0.13
Q^*_r	0.08	0.18
Q^*_l	0.07	0.18
Q^*_a	0.15	0.40

NB: Q^* = fraction of flow entering branch in relation to flow entering thoracic aorta for all input conditions

Fig. 1. Typical inlet flow waveforms, aorta model geometry, and branch flow rates.

The OSI was calculated as follows (He and Ku, 1996):

$$\mathrm{OSI} = \frac{1}{2}\left(1 - \frac{\left|\int_0^T \vec{\tau}_\mathrm{w}\,\mathrm{d}t\right|}{\int_0^T |\vec{\tau}_\mathrm{w}|\,\mathrm{d}t}\right), \tag{9}$$

where $\vec{\tau}_\mathrm{w}$ is the instantaneous WSS vector.

A scalar field of WSS angle deviations can be expressed as

$$\phi_n = \arccos\left(\frac{\vec{\tau}_{\mathrm{w},i} \cdot \vec{\tau}_{\mathrm{w},j}}{|\vec{\tau}_{\mathrm{w},i}| \cdot |\vec{\tau}_{\mathrm{w},j}|}\right), \tag{10}$$

where the WSS vectors at the location of interest are represented by $\vec{\tau}_{\mathrm{w},i}$ for the center of the control volume surface and by $\vec{\tau}_{\mathrm{w},j}$ for four surrounding control volume surfaces. The WSSAG is a mesh-independent measure of spatial variations in the mean WSS direction and defined as follows (Hyun et al., 2000, 2001; Longest and Kleinstreuer, 2000):

$$\mathrm{WSSAG} = \frac{D}{\pi}\frac{1}{T}\int_0^T |\nabla\phi_n|\,\mathrm{d}t. \tag{11}$$

When monocyte adhesion patterns are quantified, the normalized deposition fraction can be expressed as

$$\chi_{\mathrm{df}} = \frac{n\,\mathrm{d}A_{\mathrm{local}}}{\int n\,\mathrm{d}A_{\mathrm{local}}}, \tag{12}$$

where n represents the total number of computed depositions or cell adhesions in a local area $\mathrm{d}A_{\mathrm{local}}$.

The numerical calculations were carried out with a validated finite volume-based algorithm CFX 4.4 (AEAT, 2001) with user-supplied FORTRAN subroutines. Fig. 1b shows the finite volume structured surface mesh of the abdominal aorta, after testing for mesh-independence of the velocity results. The convergence of the iterations, $\varepsilon \leqslant 10^{-4}$, is controlled by the mass source residual in concert with the velocity, i.e., momentum residual. The time step size ranged from $\Delta t_{\min} = 0.0001$ s to $\Delta t_{\max} = 0.015$ s, to capture the input pulses and resulting flow structures correctly.

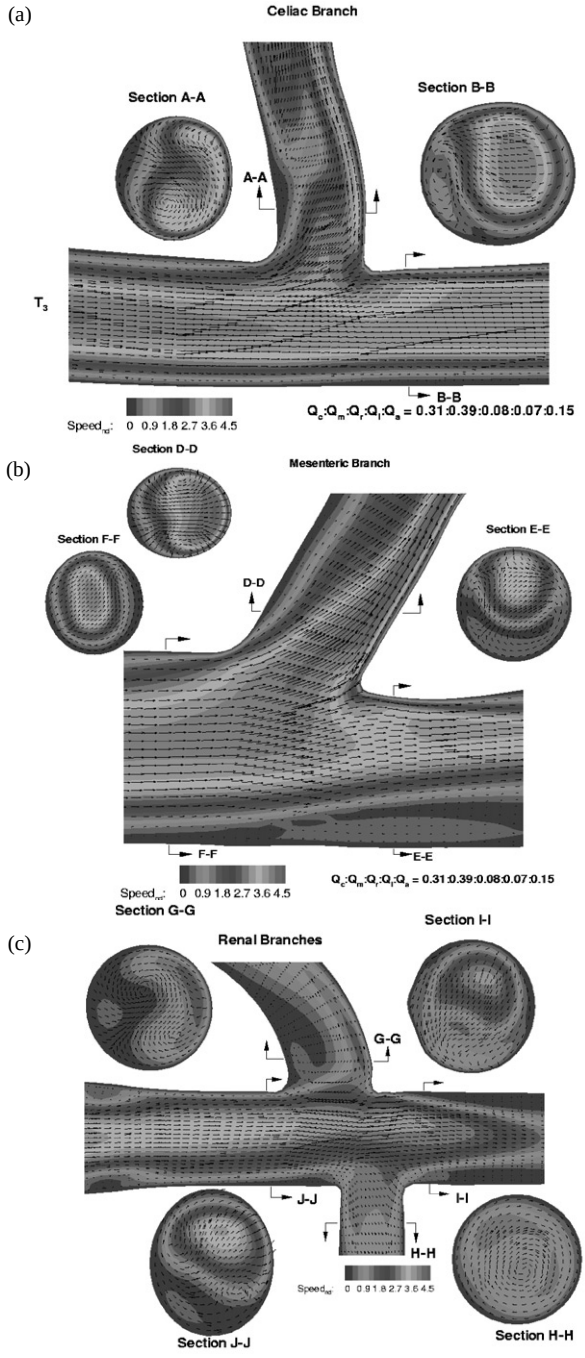

Fig. 2. Velocity fields for the resting pulse ($Re_{\mathrm{mean}} = 224$) in (a) the aorta–celiac junction; (b) mesenteric branch; and (c) renal branches.

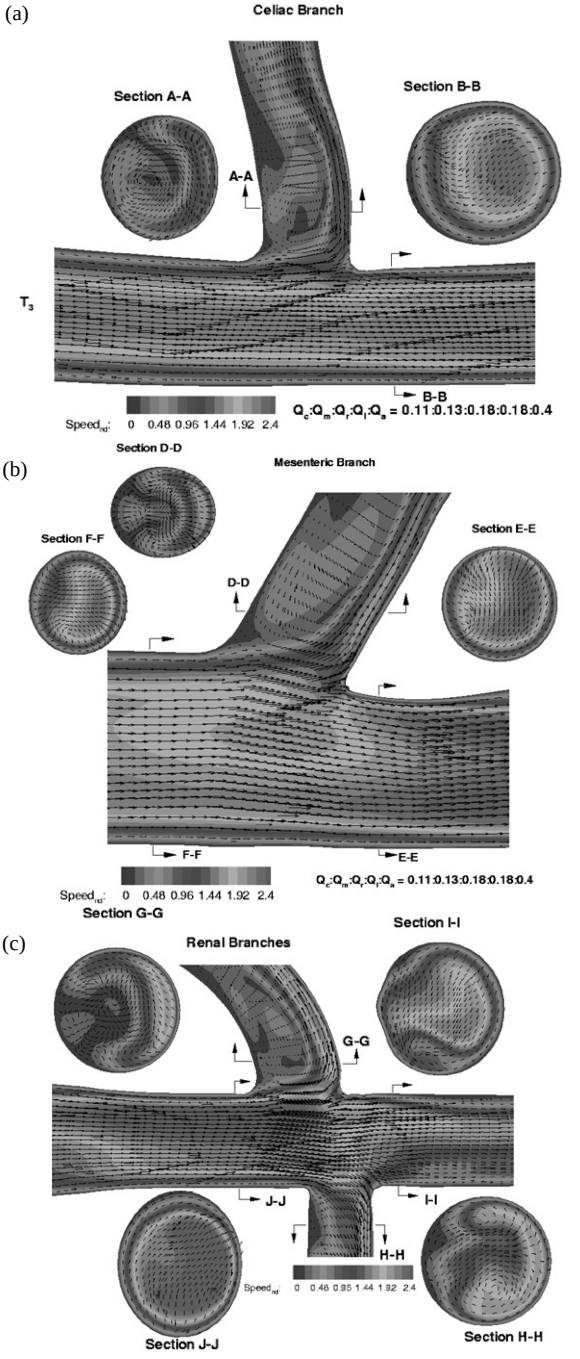

Fig. 3. Velocity fields for the exercise pulse ($Re_{\mathrm{mean}} = 700$) in (a) the aorta–celiac junction; (b) mesenteric branch; and (c) renal branches.

3. Results

The *qualitative*, or visual, indicator of "disturbed flow" are the velocity fields in (a) the aorta–celiac junction; (b) mesenteric branch; and (c) renal branches shown in Fig. 2 for the resting pulse and in Fig. 3 for the exercise pulse. Flow fields during systolic deceleration ($t = T_3$ in Fig. 1a) for the resting pulse show that secondary flows are typically amplified due to a steep decrease in inertia. Specifically, secondary flows develop along the left side near the celiac and mesenteric junctions, forming and strengthening vortices. Secondary flows persist all the way to the renal branches as indicated in cross-sections J–J and I–I. As can be expected, the flow field changed measurably for the exercise pulse, which has a biphasic waveform without a retrograde portion during diastole and a significantly higher mean Reynolds number and frequency, when compared to the resting pulse. Accompanying these differences in waveform characteristics are the branch flow rate divisions away from the celiac and mesenteric and towards the renal arteries as well as the aortic bifurcation (table in Fig. 1b).

Quantitative indicators of "disturbed flow" are time-averaged HWPs depicted in Fig. 4 for the entire abdominal aorta under resting pulse condition. Specifically, near the branch ostia, the WSS-values are elevated along the flow divider and very low lateral to the celiac and mesenteric junction, which implies lateral flow separation. Similarly, the proximal faces of the daughter branches all have low WSS-values, indicative of flow separation zones. These observations are supported by the OSI-contours which are elevated in these regions. All of the orifices have elevated WSSG-contours, which means sustained flow acceleration and deceleration in these ring-like areas. The WSSAG is similarly distributed although spreads also away from the orifice into the lateral separation zones near the celiac and mesenteric branches. To examine the deposition patterns of 50,000 monocytes ($d_p = 14\,\mu m$, $\rho_p = 1.2\,g/cm^3$),

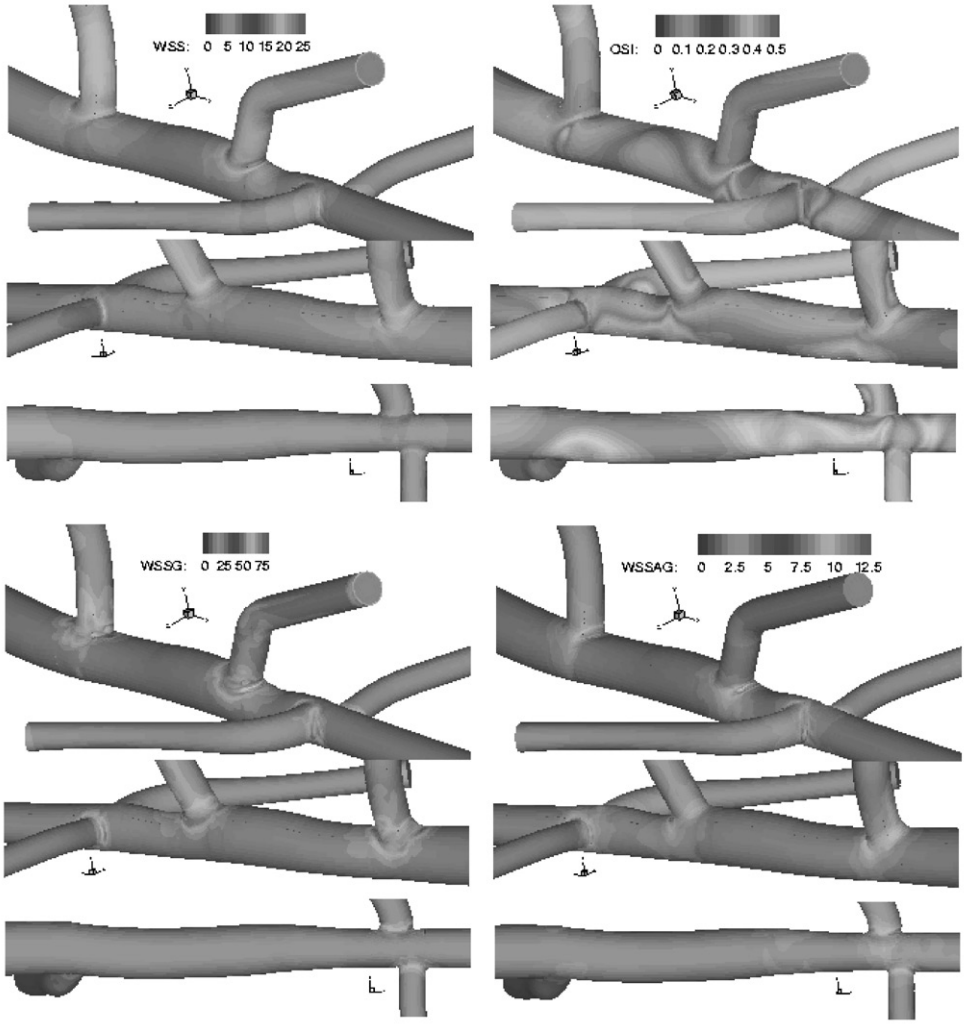

Fig. 4. Time-averaged HWPs for the resting pulse.

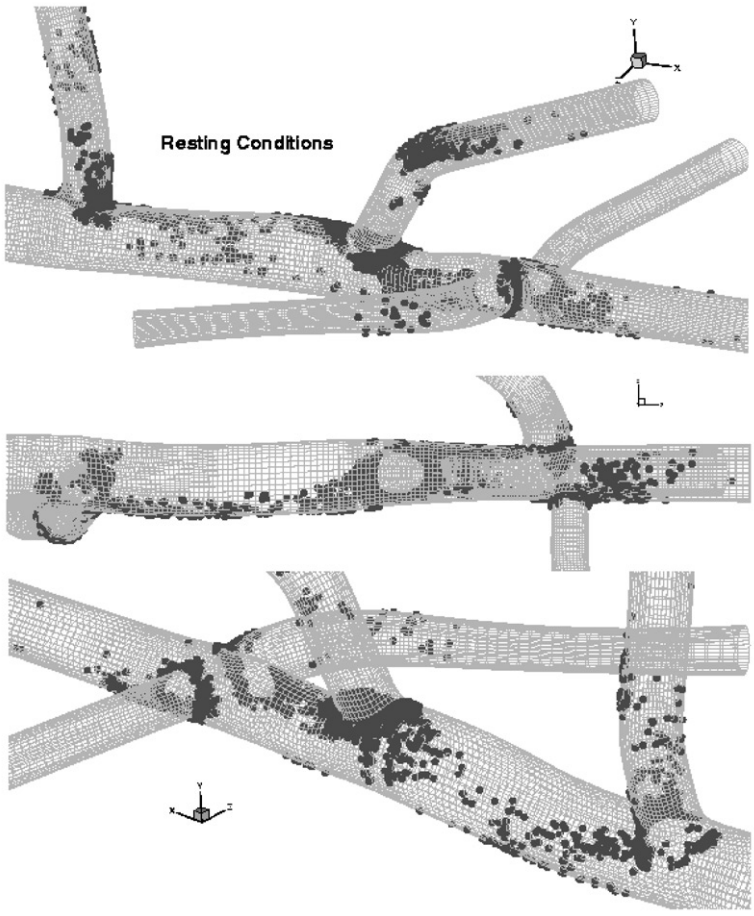

Fig. 5. Three-dimensional monocyte deposition patterns in the aorta under resting conditions.

they were tracked and adhesion was assumed when the surface of the monocyte touches the arterial wall, i.e., the cell center is within one radius to the wall. The particle deposition patterns for the resting waveform with three different views—a right distal perspective view, a dorsal view, and a left proximal perspective view—are given in Fig. 5. The deposition patterns around the additional orifices increase locally, although the mesenteric branch partially mirrors the celiac branch. A prominent feature of the deposition pattern is the curved shape it assumes as it traces down the aorta (Figs. 5, 6 and 8). It should be noted that Figs. 5 and 6 provide three-dimensional views where the dark "circles" represent cell deposition on the near or top surfaces and the lighter "circles" distant or opposite surface depositions. Measurable changes in deposition pattern occurred for the exercise pulse (Fig. 6). With the strong axial flow in the aorta and higher flow rates in the renal branches, more cells impact in the renal branch areas. In addition, there is a region of increased deposition in the left dorsal area opposite to the upstream region of the mesenteric orifice, which is due to secondary flow that develops focally during the later half of the exercise pulse (Fig. 3).

Although the exercise conditions can have a significant influence on the HWP distributions, including monocyte deposition, resting flow is more representative of the majority time spent. For easier comparison with laboratory observations, the flattened aorta is shown again with shear-stress-dependent HWP contours (Fig. 7) and wall particle distributions (Fig. 8) for the resting flow input waveform. The highest shear stresses are seen along the proximal and distal regions of the ostia and, for the most part, these regions correspond to low OSI-values. High-OSI-and-low-WSS combinations are present lateral to the celiac and mesenteric branches plus a region in the aorta between the celiac and mesenteric branches. On the dorsal wall of the aorta, the interrelationship among the secondary flows between the mesenteric and the two renal arteries is apparent as well. Opposite the mesenteric branch, the two lateral secondary flows generated by the large branch flow rate connect along the dorsal surface and continue down to the left of the dorsal cut until they connect into the lateral separation generated by the right renal branch. Similarly, separation region proximal to the left renal orifice along the dorsal wall can be seen on both the left and right sides of the flattened surface. The

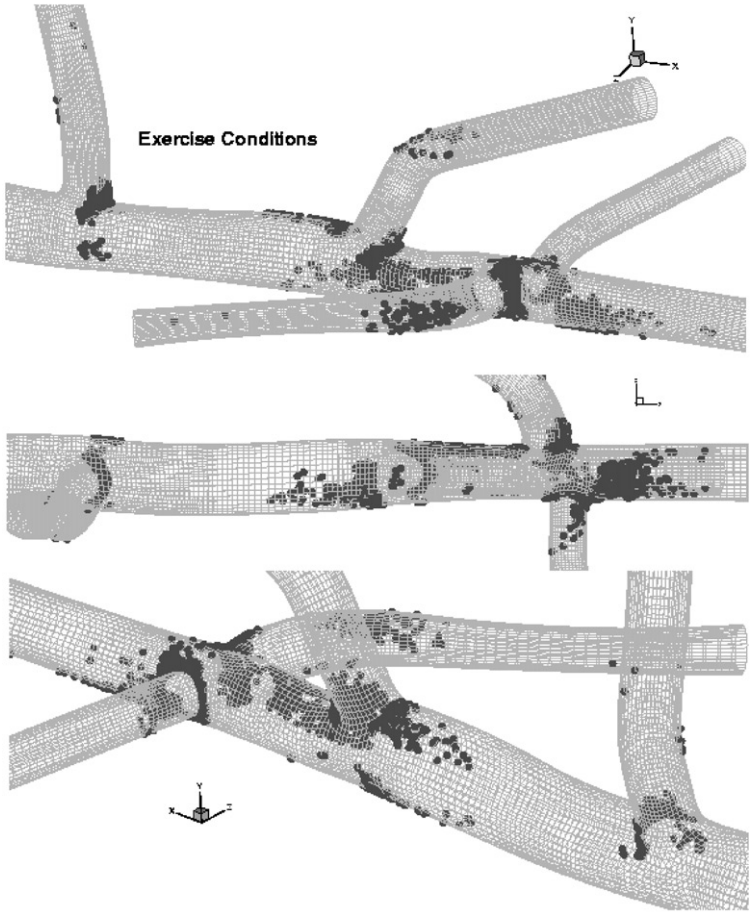

Fig. 6. Three-dimensional monocyte deposition patterns in the aorta under exercise conditions.

gradient-based parameters, the WSSG and WSSAG, are both focal, with the highest values observed near the branch orifices. The WSSAG also extends into the lateral regions near the celiac and mesenteric branches in the regions of early flow separation, and connects these two branches together as well because of the large flow disturbances near the renal branches.

In the simulated deposition pattern, a helical structure is clearly evident (Fig. 8) beginning at the celiac orifice and tracing down the left ventral side of the aorta and then sweeping through the mesenteric orifice towards the right side and connecting back through the dorsal surface into the proximal aorta distal to the renal branches. The highest numbers of deposited particles are seen near the celiac and mesenteric flow dividers, although elevated number regions appear on the proximal lip of these orifices, near the renal ostia and along the helical pattern as well.

Through the course of 4 weeks on a cholesterol diet, lesions appear attached to the lateral regions of all the orifices in approximately 1 week (data not shown) and progress to the distal lip by 2 weeks (Figs. 9a–d from Figs. 5–8 of Zeindler et al., 1989). By 4 weeks, there are occasional proximal lesions. Clearly, the early lateral development corresponds to a region of elevated OSI and low WSS for the celiac branch and this assertion carries over to the other branches although the proximity of the left renal to the right renal skews the elevated OSI to near the distal lip in this model. The continued growth of the lesions on the distal and proximal regions and along the lateral wall of the aorta is likely due to modifications in the permeability as can be related to the disturbed flows in the junction region. Increases in the WSSG, WSSAG, and χ_{df} can be noted in these regions for both the proximal and distal faces with a significant bias in the downstream direction with the exception of the proximal lip of the mesenteric artery.

The previous observations (Figs. 4–9) can be summarized with two correlations between experimental measurement data and HWP values (Figs. 10a and b). Thus, for such quantitative comparisons, the study of Malinauskas et al. (1995) is revisited considering the complete abdominal aorta. Previously, we found that r^2 for the segmental averages was 0.783 ($p = 0.0459$) when the most distal segment was excluded

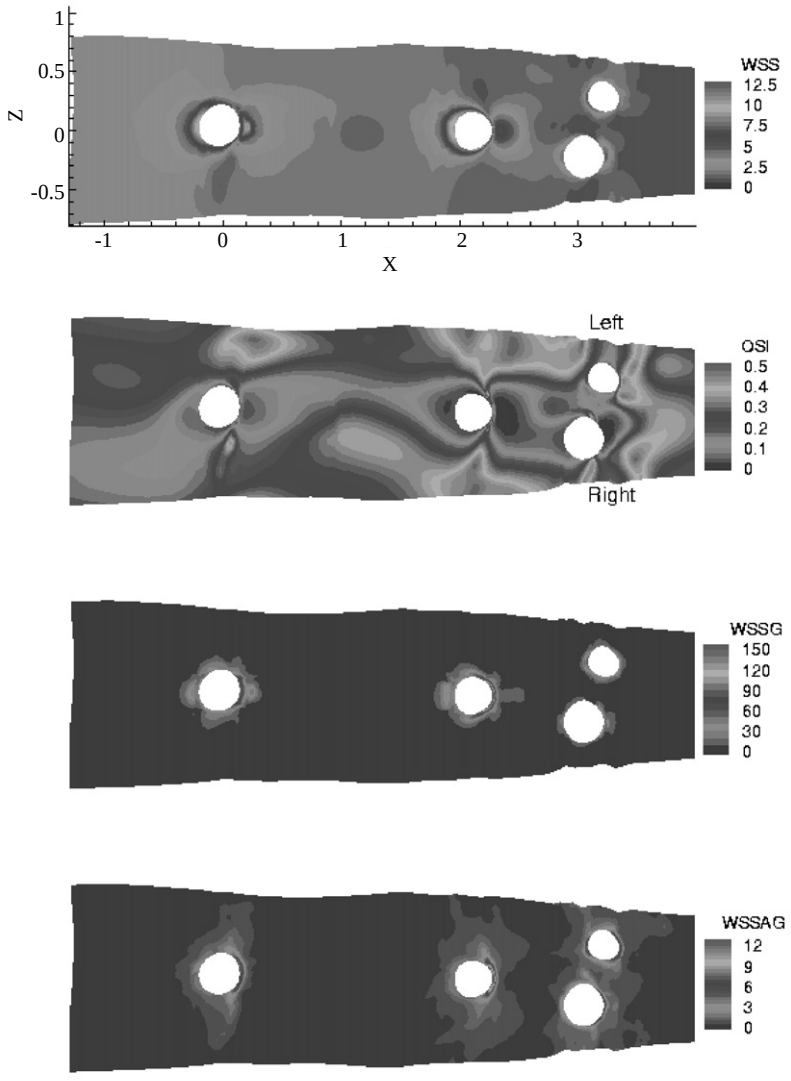

Fig. 7. HWPs in the aorta for resting flow conditions.

because the flow simulation included only the celiac branch (Buchanan et al., 1999). Now with all of the abdominal branches in the simulations and all of the segment data from Malinauskas et al. (1995), we yield r^2 equal to 0.932 for the $\langle \text{WSSG} \rangle$ ($p<0.0001$). The $\langle \text{WSSAG} \rangle$ and χ_{df} are significantly correlated with intimal white blood cells (r^2 equal to 0.755 ($p<0.01$) and 0.814 ($p<0.005$), respectively). Further, $\langle \text{WSSG} \rangle$ and $\langle \text{WSSAG} \rangle$ are significantly correlated with χ_{df} (cf. Fig. 10b).

4. Discussion

It is generally accepted that a locally dysfunctional endothelium and monocyte migration into the arterial wall are precursors of atherosclerotic lesion developments. Selecting the rabbit's abdominal aorta with several branches as an atherosclerotic model, we employed computational fluid-particle dynamics tools to simulate monocyte transport and deposition in the aorta and analyzed HWPs which predict actual sites of aggravating flow events and monocyte depositions. Specifically, we found that to a first-order approximation, monocyte contact with the endothelium is well correlated with the distribution of intimal monocyte/macrophages present in the normal and hypercholesterolemic rabbit abdominal aorta. The deposition pattern is sensitive to the waveform and reduced deposition was seen under a resting waveform. Further, both the WSSG and the WSSAG exhibit a significant correlation with the monocyte deposition parameter χ_{df} (Fig. 10b) which supports the second hypothesis that monocyte depositions can be correlated with HWPs. These HWPs describe features of disturbed flow and indicate sites of atherosclerotic lesion formation.

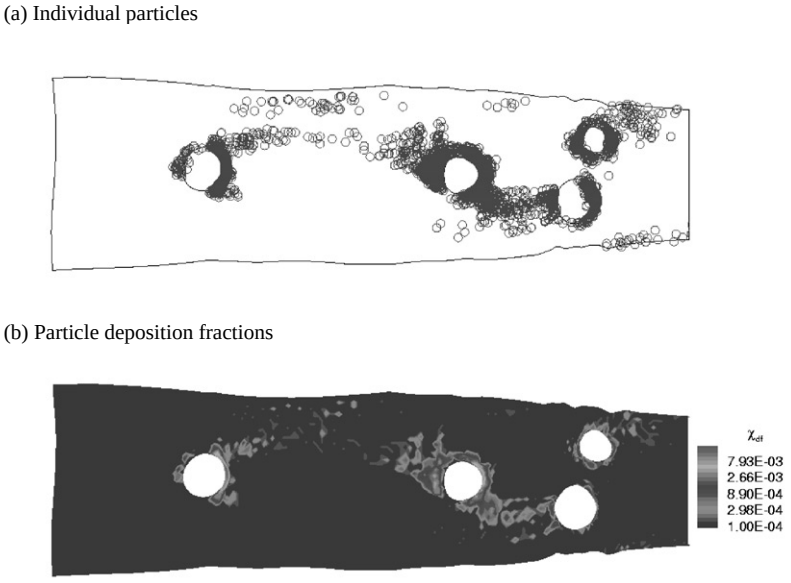

Fig. 8. Two-dimensional monocyte distribution on the aortic surface for resting flow conditions: (a) individual particles and (b) particle deposition factors.

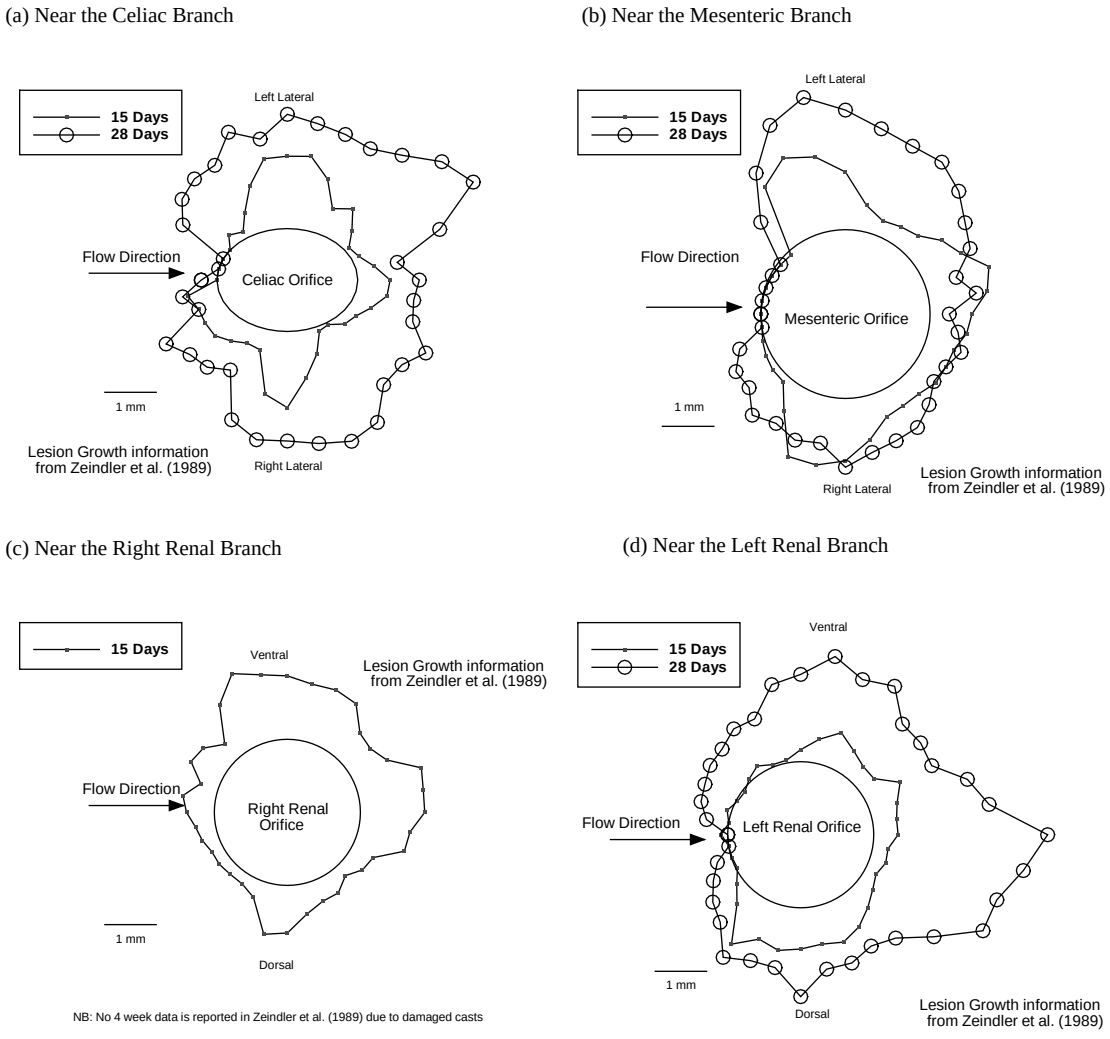

Fig. 9. Polar map demonstrating the time course of lesion growth in the aorta of cholesterol-fed rabbit.

(a) Correlations between measured WBC/monocyte densities and computed wall-shear-stress and cell-deposition based HWPs.

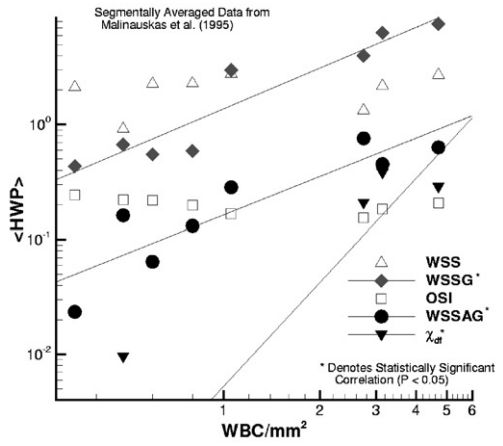

(b) Correlations between HWPs and monocyte deposition fraction.

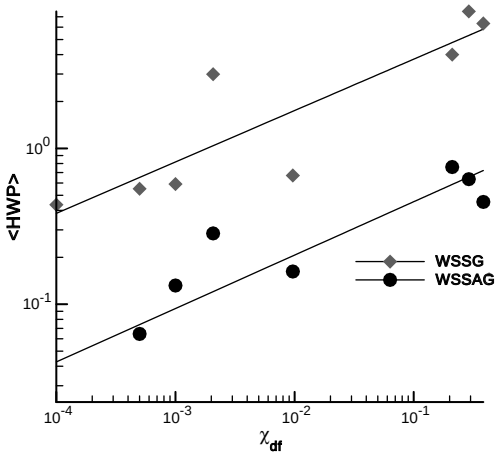

Fig. 10. Comparisons: (a) correlations between measured WBC/monocyte densities (Malinauskas et al., 1995) and computed WSS and cell-deposition-based HWPs; and (b) correlations between HWPs and monocyte deposition fraction χ_{df}.

The most prominent features of the deposition pattern are the curved shape along the aortic wall and the density elevation around vessel branches. Such distributions caused by helical flow structures in the aorta (Franzin et al., 1996) have been noted by Barakat et al. (1997). The distribution of sites of elevated permeability (Barakat et al., 1992) and intimal macrophages (Malinauskas et al., 1995) also follow this pattern of flow structures in the aorta.

One significant discrepancy between the predicted and observed monocyte deposition patterns occurs along the proximal lip of the mesenteric artery. Fluid mechanically, this region has a moderately high shear stress, elevated shear stress gradient and significant amounts of suspended elements available for incorporation. But little, if any lesion growth is noted on this face of the mesenteric. This may be due to the fact that this region is often involved in the formation of the ventral streak (cf. Barakat et al., 1992; or WBC distributions in Fig. 5 of Malinauskas et al., 1995), a region of elevated permeability that connects the celiac and mesenteric branches. This is characterized as a "gross" response and cannot be quantified on a polar mapping. To account for lesion formation that connects multiple orifices or regions that develop not attached to the orifice, probability-mapping methods, such as those of Ivey et al. (1995) as well as Barnes and Weinberg (1998, 1999), have been used to account for these fatty streak developments.

Limitations of the analysis are that it does not include the iliacs which are far downstream from the aortic segment of interest, does not examine particle–wall interactions such as cell rolling on the arterial wall, resuspension, etc., and does not account for red blood cell (RBC) collisions with monocytes. Particle–wall interaction, or the probability of adhesion, depends upon the bond strength, the force per bond and the bond-loading rate (Zhu, 2000). RBC interactions with leukocytes may change the particle trajectories and could lead to increased frequency of adhesion of cells that make contact with endothelium expressing adhesion molecules (Melder et al., 1995). Consequently, RBC–monocyte interactions would increase the probability of adhesion. These are factors that should be considered in a more detailed study.

HWPs such as the WSS, the WSSG and the WSSAG are associated with the development of atherosclerosis. These parameters may represent the influence of the local flow field upon monocyte transport, dysfunctional endothelium, and ultimately cell adhesion to endothelium. Indeed, in vitro (Barber et al., 1998; Hinds et al., 2001) and in situ studies (Ramos et al., 1999) indicate that monocyte adhesion to endothelium is influenced by the local flow field. Recent in vitro experiments (Rinker et al., 2001) and simulations (Zhao et al., 2001) show that normal forces arising from disturbed flows enhance monocyte adhesion to the arterial endothelium. Such studies may explain the correlation observed between monocyte deposition and HWPs (Figs. 10a and b).

The results of this analysis indicate that monocyte transport to the arterial endothelium is a critical factor in the localization of atherosclerosis. These findings provide further support for the view that disturbed flows, i.e., abnormal hemodynamics, affect various steps in the disease process in different ways. Monocyte deposition pattern to endothelium may be influenced by both changes in shear stresses and secondary flows arising near vessel branches.

Acknowledgements

The authors thank National Institutes of Health (Grant No. R1HL41372) for financial support of

J.R. Buchanan and S. Hyun and NIH Grant HL 577446. Use of the software CFX 4 from AEA Technology Engineering Software, Inc. (Pittsburgh, PA) and access to the SGI 2400 at the North Carolina Supercomputing Center (RTP, NC) are gratefully acknowledged.

References

AEAT, 2001. CFX-4 Users Manuals for Version 4.4. AEA Technology, Pittsburgh, PA.

Barakat, A.I., Uhthoff, P.A.F., Colton, C.K., 1992. Topographical mapping of sites of enhanced HRP permeability in the normal rabbit aorta. Journal of Biomechanical Engineering 114, 283–292.

Barakat, A.I., Karino, T., Colton, C.K., 1997. Microcinematographic studies of flow patterns in the excised rabbit aorta and its major branches. Biorheology 34 (3), 195–221.

Barber, K.M., Pinero, A., Truskey, G.A., 1998. Effects of recirculating flow on U-937 cell adhesion to human umbilical vein endothelial cells. American Journal of Physiology—Heart and Circulatory Physiology 275, H591–H599.

Barnes, S.E., Weinberg, P.D., 1998. Contrasting patterns of spontaneous aortic disease in young and old rabbits. Arteriosclerosis, Thrombosis and Vascular Biology 18, 300–308.

Barnes, S.E., Weinberg, P.D., 1999. Two patterns of lipid deposition in the cholesterol-fed rabbit. Arteriosclerosis, Thrombosis and Vascular Biology 19, 2376–2386.

Bocan, T.M.A., Mueller, S.B., Mazur, M.J., Uhlendorf, P.D., Brown, E.Q., Kieft, K.A., 1993. The relationship between the degree of dietary-induced hypercholesterolemia in the rabbit and atherosclerotic lesion formation. Atherosclerosis 102 (1), 9–22.

Buchanan Jr., J.R., Kleinstreuer, C., Truskey, G.A., Lei, M., 1999. Relation between non-uniform hemodynamics and sites of altered permeability and lesion growth at the rabbit aorto–celiac junction. Atherosclerosis 143, 27–40.

Buchanan Jr., J.R., Kleinstreuer, C., Comer, J.K., 2000. Rheological effects on pulsatile hemodynamics in a stenosed tube. Computers and Fluids 29 (6), 694–698.

Daley, S.J., Herderick, E.E., Cornhill, J.F., Rogers, K.A., 1994. Cholesterol-fed and casein-fed rabbit models of atherosclerosis, Part 1: differing lesion area and volume despite equal plasma cholesterol levels. Arteriosclerosis and Thrombosis 14, 95–104.

Davis, P.F., Mundel, T., Barbee, K.A., 1995. A mechanism for heterogeneous endothelial responses to flow in vivo and in vitro. Journal of Biomechanics 28 (12), 1553–1560.

DeBakey, M.E., Lawrie, M.G., Glaeser, D.H., 1985. Patterns of atherosclerosis and their surgical significance. Annals of Surgery 201, 115–131.

Frangos, S.G., Gahtan, V., Sumpio, B., 1999. Localization of atherosclerosis—role of hemodynamics. Archives of Surgery 134 (10), 1142–1149.

Franzin, L.J., Vonesh, M.J., Chandran, K.B., Shipkowitz, T., Yaacoub, A.S., McPherson, D.D., 1996. Confirmation and initial documentation of thoracic and abdominal aortic helical flow: an ultrasound study. ASAIO Journal 42, 951–956.

He, X., Ku, D.N., 1996. Pulsatile flow in the human left coronary artery bifurcation: average conditions. Journal of Biomechanical Engineering 118, 74–82.

Herrmann, R.A., Malinauskas, R.A., Truskey, G.A., 1994. Characterization of sites with elevated LDL permeability at intercostal, celiac and iliac branches of the normal rabbit aorta. Arteriosclerosis and Thrombosis 14, 313–323.

Hinds, M.T., Park, Y.J., Jones, S.A., Giddens, D.P., Alevriadou, B.R., 2001. Local hemodynamics affect monocytic cell adhesion to a three-dimensional flow model coated with E-selectin. Journal of Biomechanics 34 (1), 95–103.

Hyun, S., Kleinstreuer, C., Archie Jr., J.P., 2000. Hemodynamics analyses of arterial expansions with implications to thrombosis and restenosis. Medical Engineering and Physics 22 (1), 13–27.

Hyun, S., Kleinstreuer, C., Archie Jr., J.P., 2001. Computational particle hemodynamics analysis and geometric reconstruction after carotid endarterectomy. Computers in Biology and Medicine 31 (5), 365–384.

Ivey, J., Roach, M.R., Kratky, R.G., 1995. A new probability mapping method to describe the development of atherosclerotic lesions in cholesterol-fed rabbits. Atherosclerosis 115, 73–84.

Kleinstreuer, C., 1997. Engineering Fluid Dynamics—An Interdisciplinary Systems Approach. Cambridge University Press, New York.

Kleinstreuer, C., 2003. Two-phase Flow—Theory and Applications. Taylor and Francis, New York, NY and London, UK.

Kleinstreuer, C., Hyun, S., Buchanan, J.R., Longest, P.W., Archie Jr., J.P., Truskey, G.A., 2001. Hemodynamic parameters and early intimal thickening in branching blood vessels. Critical Reviews in Biomedical Engineering 29 (1), 1–64.

Longest, P.W., Kleinstreuer, C., 2000. Computational haemodynamics analysis and comparison study of arterio-venous grafts. Journal of Medical Engineering and Technology 24 (3), 102–110.

Malinauskas, R.A., Herrmann, R.A., Truskey, G.A., 1995. The distribution of intimal white blood cells in the normal rabbit aorta. Atherosclerosis 115, 147–163.

Malinauskas, R.A., Sarraf, P., Barber, K.M., Truskey, G.A., 1998. Association between secondary flow in models of the aorto-celiac junction and subendothelial macrophages in the normal rabbit. Atherosclerosis 140, 121–134.

Melder, R.J., Munn, L.L, Yamada, S., Ohkubo, C., Jain, R.K., 1995. Selectin- and integrin-mediated T-lymphocyte rolling and arrest on TNF-α-activated endothelium: augmentation by erythrocytes. Biophysical Journal 69, 2131–2138.

Nerem, R.M., 1992. Vascular fluid mechanics, the arterial wall and atherosclerosis. Journal of Biomechanical Engineering 114, 274–282.

Olsson, A.G., 1987. Atherosclerosis: Biology and Clinical Science. Churchill Livingstone.

Pedersen, E.M., Oyre, S., Agerbaek, M., Kristensen, I.B., Ringgaard, S., Boesiger, P., Paaske, W.P., 1999. Distribution of early atherosclerotic lesions in the human abdominal aorta correlates with wall shear stresses measured in vivo. European Journal of Vascular and Endovascular Surgery 18 (4), 328–333.

Popel, A.S., Enden, G., 1993. An analytic solution for steady flow of Quemada fluid in a circular tube. Rheologica Acta 32, 422–426.

Ramos, C.L., Huo, Y.Q., Jung, US, Ghosh, S., Manka, D.R., Sarembock, I.J., Ley, K., 1999. Direct demonstration of P-selectin-and VCAM-1-dependent mononuclear cell rolling in early atherosclerotic lesions of apolipoprotein E-deficient mice. Circulation Research 84 (11), 1237–1244.

Rinker, K.D., Prabhakar, V., Truskey, G.A., 2001. Effect of contact time and force on monocyte adhesion to vascular endothelium. Biophysical Journal 80, 1722–1732.

Ross, R., 1993. The pathogenesis of atherosclerosis: a perspective for the 1990s. Nature 362, 801–809.

Texon, M., 1996. Hemodynamic basis of atherosclerosis with critique of the cholesterol—heart disease hypothesis, 2nd Edition. Begell House Publishers, New York.

Truskey, G.A., Herrmann, R.A., Kait, J., Barber, K.M., 1999. Focal increases in VCAM-1 and intimal macrophages at atherosclerosis-susceptible sites in the rabbit aorta after short-term cholesterol feeding. Arteriosclerosis, Thrombosis and Vascular Biology 19, 393–401.

Womersley, J.R., 1955. Method for the calculation of velocity, rate of flow and viscous drag in arteries when their pressure gradient is known. Journal of Physiology 127, 553–563.

Zeindler, C.M., Kratky, R.G., Roach, M.R., 1989. Quantitative measurements of early atherosclerotic lesions on rabbit aortae from vascular casts. Atherosclerosis 76, 245–255.

Zhao, Y., Chien, S., Weinbaum, S., 2001. Dynamic contact forces on leukocyte microvilli and their penetration of the endothelial glycocalyx. Biophysical Journal 80, 1124–1140.

Zhu, C., 2000. Kinetics and mechanics of cell adhesion. Journal of Biomechanics 33, 23–33.